ACS APPLIED NANO MATERIALS

www.acsanm.org Article

Amorphous-to-Crystal Transition in Quasi-Two-Dimensional MoS_2: Implications for 2D Electronic Devices

Milos Krbal,* Vit Prokop, Alexey A. Kononov, Jhonatan Rodriguez Pereira, Jan Mistrik, Alexander V. Kolobov, Paul J. Fons, Yuta Saito, Shogo Hatayama, Yi Shuang, Yuji Sutou, Stepan A. Rozhkov, Jens R. Stellhorn, Shinjiro Hayakawa, Igor Pis, and Federica Bondino

Cite This: *ACS Appl. Nano Mater.* 2021, 4, 8834–8844 Read Online

ACCESS | Metrics & More | Article Recommendations

ABSTRACT: Two-dimensional (2D) transition metal dichalcogenides (TMDCs) have demonstrated a very strong application potential. In order to realize it, the synthesis of stoichiometric 2D TMDCs on a large scale is crucial. Here, we consider a typical TMDC representative, MoS_2, and present an approach for the fabrication of well-ordered crystalline films *via* the crystallization of a thin amorphous layer by annealing at 800 °C, which was investigated in terms of long-range and short-range orders. Strong preferential crystal growth of layered MoS_2 along the ⟨002⟩ crystallographic plane from the as-deposited 3D amorphous phase is discussed together with the mechanism of the crystallization process disclosed by molecular dynamic simulations using the Vienna Ab initio Simulation Package. We believe that the obtained results may be generalized for other 2D materials. The proposed approach demonstrates a simple and efficient way to fabricate thin 2D TMDCs for applications in nano- and optoelectronic devices.

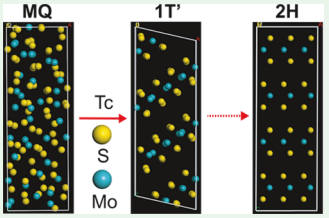

KEYWORDS: *thin films, X-ray absorption spectroscopy, MoS_2, local structure, crystallization, molecular dynamics, optical properties, XPS*

INTRODUCTION

Recent advances in nanotechnology have led to the discovery of the unique properties of two-dimensional transition metal dichalcogenides (TMDCs), which have found potential in numerous applications such as optoelectronics,[1,2] biosensors,[3] photocurrent generation,[4,5] photocatalytic degradation of organic pollutants,[6,7] electrocatalytic hydrogen evolution,[8,9] and energy storage[9,10] among others. In contrast to graphene, a monolayer of TMDC such as MoS_2 is a semiconductor with a direct band gap[11] which can be further tuned by external stimuli,[1,12,13] doping,[14,15] or by use of controlled artificial layering of 2D materials with different properties to form heterostructures.[16]

Nevertheless, the growth of compositionally uniform thin layers on a large scale still remains challenging. In general, covalently bonded TMDC layers can be easily prepared by two approaches, that is top-down and bottom-up techniques.[2] Top-down fabrication methods include mechanical and chemical exfoliation using techniques such as direct ultrasonication or ion intercalation.[17] While exfoliation is widely used to fabricate monolayers of van der Waals-based chalcogenides, the obtained layers are few and in the form of micron-sized small flakes, which strongly limit their potential use. On the other hand, bottom-up deposition methods, such as chemical vapor deposition and atomic layer deposition (ALD),[2,18,19] serve to coat a large area with free-standing or flat flakes with monolayer precision. However, the disadvantage of these techniques can be found in the necessity of using very toxic organic and/or inorganic precursors together with the difficulty of determining proper deposition conditions to obtain stoichiometric layers of TMDCs without additional contamination from organic remnants.

The stoichiometric growth of TMDCs is also challenging using near equilibrium physical deposition techniques due to the large differences in vapor pressure among the constituent elements. Therefore, two-step processes must be considered as an alternative path for fabrication of crystalline TMDCs on a large scale. Such processes include thermal decomposition of dipped or spin-coated $(NH_4)_2Mo(W)S_4$ under an inert or sulfur atmosphere,[20,21] deposition of a thin film of a transition metal[22] or a transition metal oxide[23] on a substrate in the first step and subsequent conversion of this layer to a TMDC in a vapor of chalcogen, or simply crystallization of an as-deposited amorphous thin film of TMDC. In the latter approach, the formation of the layered crystalline phase *via* transformation from a 3D continuous amorphous phase avoids nonstoichiometric growth as has been very recently demonstrated for $MoTe_2$.[24] In addition, deposition of amorphous chalcogenide

Received: June 8, 2021
Published: September 8, 2021

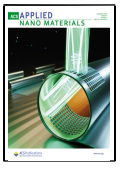

thin films has been intensively investigated for many decades, and thus, this technology can be easily transferred to nanoscale applications as demonstrated, for instance, in phase-change materials.[25]

Since there is very limited information about the physics of the amorphous-to-crystal (or 3D−2D) transformation in TMDCs, in this paper, we present a study of the amorphous and crystalline phases of MoS_2, examined in terms of long-range and short-range orders. In addition, the experimental preferential crystal growth of layered MoS_2 along the ⟨002⟩ direction from the as-deposited amorphous phase is discussed based upon X-ray diffraction (XRD) measurements. The underlying mechanism of the crystallization process is then explored by means of *ab initio* molecular dynamic (AIMD) simulations. The proposed approach demonstrates a simple and efficient way to fabricate thin 2D TMDCs for applications in nano- and optoelectronic devices.

EXPERIMENTAL DETAILS

Amorphous MoS_2 films were deposited at room temperature using radio-frequency magnetron sputtering onto silica and silicon substrates. The thickness of the as-deposited films was about 50 nm. To prevent sample oxidation during crystallization, a part of the sample was placed into a clean quartz ampoule, which was subsequently evacuated to 10^{-3} Pa and sealed. The crystallization process was subsequently carried out in a furnace with a 2 °C/min heating rate, heating the sample at 800 °C for 1 h and then allowing it to naturally cool down to room temperature (see Figure 1).

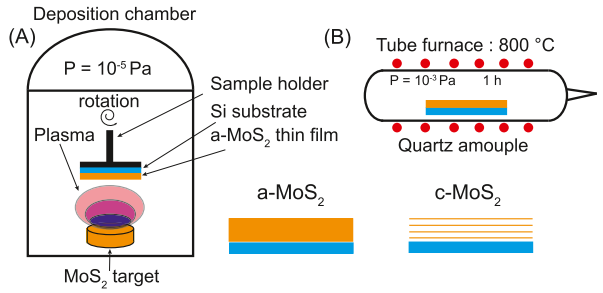

Figure 1. (Color online) (A) Schematic showing a deposition of amorphous MoS_2 thin films using magnetron sputtering. (B) Schematic showing crystallization of the amorphous MoS_2 thin film at 800 °C under a residual pressure of 10^{-3} Pa.

XRD measurements were carried out on both amorphous and crystalline samples of MoS_2, including the MoS_2 powder as a reference sample, using a diffractometer (Empyrean Malvern Panalytical) operating in two-theta/omega mode to fully satisfy the Bragg−Brentano geometry. Background subtraction was performed using the FullProf software package[26] to remove the contribution to the XRD signal from the substrate.

Ellipsometric spectra were recorded using a VASE ellipsometer (Woollam Co. Ltd.) over a spectral range 0.7−6.5 eV. The angle of incidence was varied from 50 to 80° in 10° steps. The obtained spectra were simultaneously fitted with optical reflectivity measured using the same instrument. The fitting model consisted of a c-Si semi-infinite substrate covered with SiO_2, a native oxide, and a MoS_2 single layer. The surface roughness was considered by means of the Bruggeman effective medium approximation with a mixture of 50% voids and 50% MoS_2. The optical constants of the polycrystalline (amorphous) MoS_2 film were parameterized by a sum of eight (three) Gaussian oscillators.

Surface compositional analyses were carried out by X-ray photoelectron spectroscopy (XPS, ESCA2SR, Scienta-Omicron) using a monochromatized Al Kα (1486.7 eV) X-ray source. The binding energy scale was normalized to the adventitious carbon peak located at 284.8 eV. The spectra were fitted using Shirley-type background removal and Gaussian and Lorentzian functions. Mo 3d and S 2p doublet separations were fixed at 3.14 and 1.19 eV, respectively. These values were determined by fitting the MoS_2 reference sample spectra.

Mo K-edge X-ray absorption spectroscopy (XAS) for the as-deposited and crystalline samples was performed at a low temperature (10 K) in fluorescence mode using grazing incidence geometry at the beamline BL01B1 at SPring-8. S K-edge XAS spectra were measured at the beamline BL11 at the Hiroshima Synchrotron Radiation Center (HiSOR). The experiment was conducted in a He atmosphere, at room temperature. S $L_{2,3}$ X-ray absorption was carried out at the BACH beamline of CNR at the Elettra synchrotron facility. XAS measurements were performed in total electron yield by measuring the drain current through the sample using a picoammeter. S $L_{2,3}$ XAS spectra were acquired using linearly polarized radiation with a polarization vector 80° off the surface plane. The photon energy resolution was set to 75 meV. XAS data were processed and fitted using Athena and Arthemis software packages.[27]

The melt-quenched (MQ) amorphous phase of MoS_2 was generated *via* molecular dynamics using the Vienna ab initio simulation package (VASP).[28] Projector-augmented wave pseudopotentials that included the electron configurations $3s^2$ $3p^4$ and $4d^5$ $5s^1$ as valence states for S and Mo, respectively, were used. The PBE exchange−correlation functional[29] was used with a plane-wave basis and with a cutoff energy of 260 eV. The initial 108 atom cell (the 2H phase containing 36 and 72 atoms of Mo and S, respectively) was randomized at 5000 K for 10 ps to reach a molten phase. The temperature of the structure was subsequently decreased to 2200 K in another 10 ps and maintained at this temperature for 10 ps to obtain an equilibrate state and then quenched to 200 K in 10 ps. The crystallization of MQ-MoS_2 was performed at 1800 K for 200 ps.

X-ray absorption near-edge structure (XANES) spectra were calculated using the *ab initio* real-space full multiple-scattering code FEFF9.[30] FEFF is a fully relativistic, all-electron Green function code that utilizes a Barth-Hedin formulation for the exchange−correlation part of the potential and Hedin−Lundqvist self-energy correction. In our FEFF calculations, the cluster radius was set to 9 Å around the central atom, which corresponds to about 108 atoms in the model used. The XANES spectra were calculated for each of the 36 Mo and 72 S atoms in the unit cell and subsequently averaged for comparison with the experimental data.

RESULTS AND DISCUSSION

Figure 2 shows XRD patterns of as-deposited (a-MoS_2) and annealed (c-MoS_2) thin films of MoS_2 at 800 °C. One can see from Figure 2 that there is no evidence of distinct Bragg reflection peaks in a-MoS_2, which confirms its amorphous character. On the other hand, the XRD pattern of the c-MoS_2 sample is characterized by a single reflection peak at $2\theta = 14.3°$

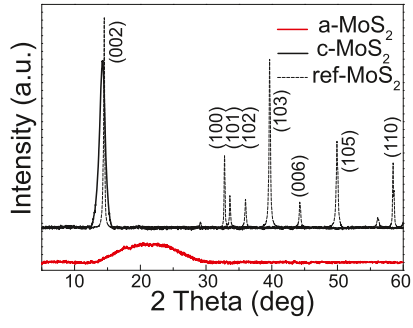

Figure 2. (Color online) XRD patterns of the as-deposited and crystallized MoS_2 thin films. The dashed line represents a MoS_2 powder sample as the reference material.

https://doi.org/10.1021/acsanm.1c01504
ACS Appl. Nano Mater. 2021, 4, 8834−8844

across the whole 2θ range from 5 to 60°, which corresponds to an interlayer distance of 6.2 Å along the *c*-axis,[31] a typical value for c-MoS_2. In comparison with the powder diffraction pattern of the reference MoS_2 sample, the reflection peak is a good fit to the most intensive reflection peak along the ⟨002⟩ crystallographic plane, which indicates that we have prepared the crystalline single phase of 2H-MoS_2 upon crystallization of the initial amorphous phase. Considering that both the reference and c-MoS_2 samples are polycrystalline materials, the existence of the single reflection peak in c-MoS_2 can be attributed to strong preferential crystal growth of the 2H-MoS_2 phase with out-of-plane *c*-axis orientation along the ⟨002⟩ direction from the a-MoS_2 amorphous counterpart, which was annealed at 800 °C in a vacuum ambience. We would like to note that preferential crystallization was observed on MoS_2 samples deposited on both ⟨100⟩ Si and fused silica substrates, which underscores that such crystallization behavior is an intrinsic property of a-MoS_2 rather than being a template effect. At first glance, it is clear that the reflection peak of c-MoS_2 is distinctly broader compared to the same peak originating from the reference sample, which probably reflects the formation of a smaller grain size during crystallization of a-MoS_2 at 800 °C.

The optical properties of the as-deposited and crystallized MoS_2 films were investigated using spectroscopic ellipsometry. Figure 3 shows the resulting refractive, *n*, and extinction, *k*,

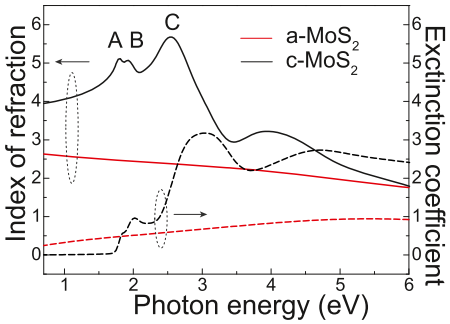

Figure 3. (Color online) Index of refraction (solid lines) and extinction coefficients (dashed lines) of the as-deposited and crystallized MoS_2 thin films.

coefficients for the corresponding MoS_2 samples. One can see that the optical constants *n* (*k*) for a-MoS_2 monotonically decrease (increase) with increasing photon energy (without excitonic features). On the other hand, the optical constants for c-MoS_2 display a clear excitonic behavior, which corresponds to the splitting of the valence band by spin orbit coupling.[2,32] The presence of excitons is associated with the symmetry of the Brillouin zone,[33] which additionally confirms the formation of the crystalline phase in c-MoS_2.

In general, sulfur-based amorphous chalcogenides, also called chalcogenide vitreous semiconductors, or chalcogenide glasses, have negligible absorption in the transparent spectral region.[34] This fact has been stressed as very unusual by Sir Nevill Mott in his Nobel lecture[35] because transparent means having an energy gap between the conduction and valence bands and the formation of such a gap has been traditionally attributed to the presence of the long-range order, which does not exist in amorphous materials. Consequently, it was demonstrated that the formation of the energy gap is determined by the short-range order and, in particular, is due to the presence of saturated covalent bonds.

This clearly is not the case for a-MoS_2. The observed strong absorption in the near-infrared spectral region indicates a high concentration of defects within the mobility gap of a-MoS_2. At the same time, it is known that many defects in the mobility gap also exist in chalcogenide glasses, such as As_2S_3, which are nonetheless highly transparent in the infrared spectral region. This unusual coexistence of a large concentration of defect states and high transparency in chalcogenide glasses was linked to the formation of the so-called valence alternation pairs (VAPs), where in addition to negatively charged dangling bonds, positively charged three-fold coordinated defects are formed due to the presence of lone-pair electrons.[36] The presence of VAPs in amorphous As_2S_3 and related materials results in the Fermi level being pinned to the midgap. In MoS_2, at least in the crystalline phase, lone-pair electrons are not present. One may thus speculate that the absence of VAPs and the existence of homopolar "metallic" Mo−Mo bonds in a-MoS_2 may be an important factor behind the presence of defect levels in the mobility gap.

While the average elemental composition was the same for both samples, we performed the XPS and XAS analyses to discern the main differences between a- and c-MoS_2 on the oxidation state and the local arrangements around Mo and S atoms. Figure 4 shows XPS spectra for the Mo 3d and S 2p core levels of the prepared a-MoS_2 and c-MoS_2 layers. The corresponding spectra from the reference MoS_2 powder are also given for comparison. It is obvious from the XPS spectra that the composition and the oxidation state distributions in the a-MoS_2 and c-MoS_2 samples are different, while the comparison of Mo 3d and S 2p core levels for the c-MoS_2 film and the MoS_2 reference sample clearly manifests very similar spectral shapes. A deeper analysis of the Mo 3d core level for a-MoS_2 disclosed that the as-deposited thin film is a mixture of three contributions of nearly equal intensity signals attributable to Mo(IV)−S in the 1T′—like symmetry (magenta) containing Mo−Mo homopolar bonds with the binding energy $E_B(3d_{5/2})$ = 228.86 eV,[37] Mo(IV)−S in the 2H—like symmetry (light blue) with $E_B(3d_{5/2})$ = 229.3 eV,[38] and molybdenum oxo-sulfides Mo(IV)−O/S (brown) with $E_B(3d_{5/2})$ = 230.3 eV.[40] MoS_2 satellites derived from final-state screening effects could also contribute to the last component.[37,41] A weak signal at high binding energies with $E_B(3d_{5/2})$ = 232.93 eV can be ascribed to the doublet of Mo(VI)−O in MoO_3 (green)[39] coming from surface oxidation after air exposure. An additional broad band ascribed to S-based units can be found at $E_B(2s)$ = 226.8 eV,[8] which is consistent with the Mo 3d XPS spectrum of MoS_2. The c-MoS_2 spectra mainly consists of the Mo(IV)−S bonds in the 2H symmetry with a small contribution of Mo(VI)−O.

Analysis of the S 2p core level led to identification of two different sulfur oxidation states in a-MoS_2, namely S(-II) with the binding energy $E_B(2p_{3/2})$ = 162.1 eV[8] and S_n(-II) with $E_B(2p_{3/2})$ = 162−163.8 eV assigned to polysulfides with a variable number of sulfur atoms in the chain.[42] On the other hand, c-MoS_2 is characterized exclusively by the S(-II) oxidation state in the 2H symmetry, which demonstrates the presence of a single crystalline phase of MoS_2. The percentage contributions of the Mo and S oxidation states observed in a- and c-MoS_2 are summarized in Table 1.

The characteristic features in the valence bands of a- and c-MoS_2 also unambiguously describe the amorphous-to-crystal

https://doi.org/10.1021/acsanm.1c01504
ACS Appl. Nano Mater. 2021, 4, 8834−8844

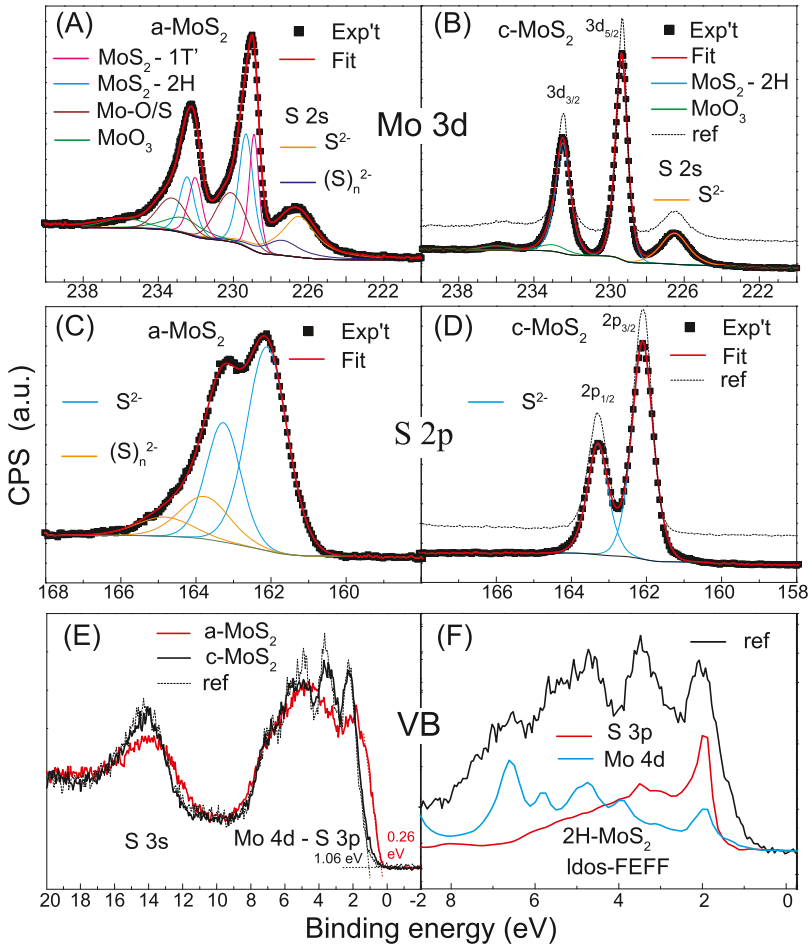

Figure 4. (Color online) XPS spectra of the as-deposited (A,C) and crystalline (B,D) MoS_2 thin films. Figure (E) shows differences in the corresponding valence band spectra and (F) calculated contributions of S 3p and Mo 4d orbitals (lDOS) to the valence band of crystalline MoS_2 in the 2H phase.

Table 1. Contribution in Percentage of Individual Components to the XPS Signal of As-Deposited, Crystallized, and Reference Powder MoS_2[a]

sample	Mo−S (1T′-like)	Mo−S (2H-like)	Mo−O/S	MoO_3	S−Mo	S_n(-II)
a-MoS_2	8.26	10.89	9.89	2.65	54.30	14.06
c-MoS_2		33.32		2.40	64.27	
powder MoS_2		30.99		3.64	65.37	

[a]The relative contributions are calculated from integrated intensities after the normalization to the corresponding Mo 3d and S 2p sensitivity factors.

transition observed in MoS_2 as shown in Figure 4E. First, the mobility gap edge of a-MoS_2 shifts by ≈0.8 eV toward lower energy compared to that of c-MoS_2, which is consistent with the aforementioned stronger absorption of a-MoS_2 in the near-infrared spectral region. Second, the valence band of the 2H reference MoS_2 sample is formed by the hybridization of Mo 4d and S 3p, which generates five major bands within the binding energy range 0−10 eV.[43] An additional band peaking at ≈14 eV is assigned to the S 3s orbitals. The contribution of the S 3p and Mo 4d states to the overall valence band structure can be understood by an examination of the local projected density of states of the 2H-MoS_2 structure, which was calculated using the FEFF code (see Figure 4F). The first band at ≈2 eV is mainly determined by S 3p orbitals with a small contribution from Mo 4d. With increasing binding energy, the band at ≈3.3 eV consists of both S 3p and Mo 4d orbitals in about the same ratio and the last three bands at ≈4.6, ≈5.4, and ≈6.6 eV are mainly due to Mo 4d orbitals. One can see from Figure 4E that the main difference in the valence band between a- and c-MoS_2 can be observed in the intensity of the first two bands that are associated with the hybridized S 3p orbitals and the intensity of S 3s orbitals. We assume that these main changes are connected to the existence of the homopolar S−S bonds in a-MoS_2 within polysulfide chains that do not form Mo−S bonds. Another explanation could be due to Mo 4d from the Mo−Mo homopolar bonds and/or Mo 4d−S 3p hybridized states from the 1T′-like structure. Note the similarities with the 1T′ phase valence band in the recent report.[44] In contrast, very similar valence band spectra for the reference and c-MoS_2 manifest the high crystalline quality of the c-MoS_2 thin film.

Complementary structural information to the XPS results was obtained by XAS, which provides information on electronic transitions around the X-ray absorption edge represented by XANES spectra as well as the coordination numbers (CNs), bond lengths (BLs), and mean-square relative displacements (MSRDs). It is important to note that XAS probes samples across the total thickness, while XPS only investigates the upper 2 nm, where the composition may

https://doi.org/10.1021/acsanm.1c01504
ACS Appl. Nano Mater. 2021, 4, 8834−8844

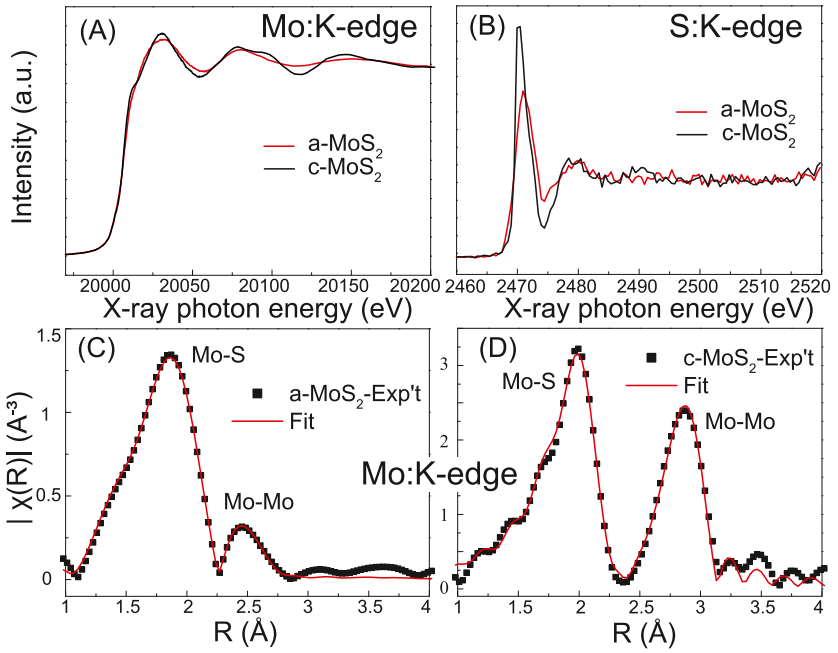

Figure 5. (Color online) Experimental (A) Mo K-edge and (B) S K-edge XANES spectra of the as-deposited amorphous and crystalline MoS_2 thin films which demonstrate a significant difference in the local structure during the phase transition. (C,D) Mo K-edge real-space fitting of EXAFS data of the as-deposited amorphous and crystalline MoS_2 thin films.

Table 2. CNs, BLs, and MSRD of As-Deposited and Crystallized MoS_2

bonds	CN	BL/Å	MSRD/Å^2	refs (BL/Å)
a-Mo−S	5.26 ± 0.28	2.41 ± 0.01	0.0085 ± 0.0005	2.43[45,46]
a-Mo−Mo	1.33 ± 0.42	2.81 ± 0.02	0.008 ± 0.002	2.77[45,46]
a-Mo−O	0.39 ± 0.32	1.62 ± 0.08		1.69[47]
c-Mo−S	6.65 ± 0.33	2.41 ± 0.01	0.002 ± 0.0003	2.41[45,46]
c-Mo−Mo	6.8 ± 0.61	3.16 ± 0.01	0.003 ± 0.0003	3.155[45,46]

change due to redeposition or spontaneous air oxidation. Figure 5A,B shows XANES spectra for both the Mo K- and S K-edges in the a- and c-MoS_2 states. Although differences are evident at both X-ray absorption edges, more pronounced changes, especially in the intensity of the "white line", can be observed at the S K-edge, suggesting that the main structural change in the local arrangement occurs around the S atoms. However, oscillations above the "white line" are also clearly visible at the Mo K-edge for both MoS_2 phases, and therefore, the change in the local structure around the Mo species also cannot be neglected.

Figure 5C,D depicts the Mo K-edge real-space fitting of EXAFS data for a- and c-MoS_2 showing the Mo−S and homopolar Mo−Mo BLs. Note that the displayed data are phase-shifted due to the effect of the atomic potentials involved in the scattering process; the phase-shifts have been accounted for in the fitting process. After data fitting using the Demeter software packages,[27] we found that the first coordination shell around the Mo atoms in as-deposited MoS_2 contains S and Mo as first nearest neighbors located at distances of 2.41 and 2.81 Å, respectively. The latter is significantly shorter than the Mo−Mo distance in the crystalline phase and indicates the formation of Mo−Mo bonds, in agreement with the XPS results.

These values are in good agreement with recent reports on a-MoS_2 prepared using different techniques such as plasma-enhanced ALD[45] and electrodeposition.[46] The analysis further reveals that partial CNs of both Mo−S and Mo−Mo bonds are 5.26 and 1.33, respectively, which suggest that approximately 20% of Mo atoms form homopolar bonds. Note that the concentrations of homopolar Mo−Mo bonds obtained from XPS and EXAFS analyses are very similar, which may imply good homogeneity of the sample throughout the film thickness. While the Mo−O bonds are at the limit of detection, their contribution noticeably improves the final fit. On the other hand, the first coordination shell of c-MoS_2 is exclusively formed by the heteropolar Mo−S bonds with an identical BL of 2.41 Å and a CN of 6.65, which is consistent with the total CN of the Mo atoms observed in a-MoS_2. Thus, we can conclude that during crystallization, the Mo−Mo bonds dissociate and new Mo−S bonds are formed.

The second nearest neighbor is represented by the Mo atoms with an interatomic distance of 3.16 Å, which unequivocally indicates the formation of 2H modification after crystallization. The results obtained from the EXAFS analysis are summarized in Table 2.

To gain deeper insights into the structure at the atomic level, we have employed a model of "MQ" amorphous MoS_2 obtained *via* AIMD simulations using the VASP code.[28] Figure 6 shows our MQ-MoS_2 structural model, which is composed of 108 atoms in the simulation cell (36 Mo atoms and 72 S atoms). By thorough analysis of the MQ structure, we constructed a distribution of bonds in the form of histograms with a bin size of 0.05 Å as demonstrated in Figure 6A−C. One can see that the Mo atoms in MQ-MoS_2 form the heteropolar Mo−S bonds with their BLs peaking at 2.4 Å and the partial

https://doi.org/10.1021/acsanm.1c01504
ACS Appl. Nano Mater. 2021, 4, 8834−8844

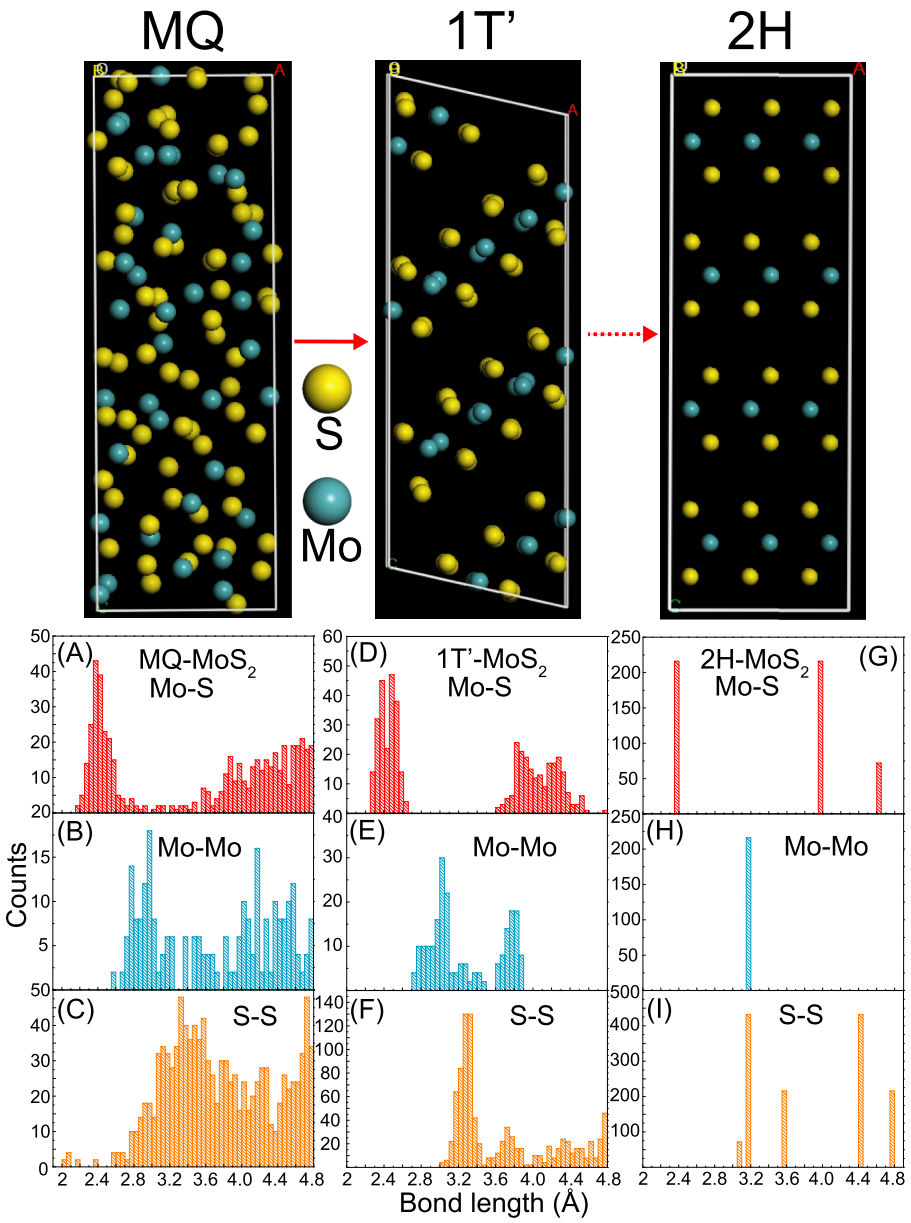

Figure 6. (Color online) MQ-MoS_2 and subsequent crystallization to the 1T′ phase *via* molecular dynamic simulation using the VASP code. The 2H-MoS_2 phase, taken from a database, represents the final stable phase. (A–I) BL analyses of the MQ-MoS_2 phase, the 1T′ phase, and the 2H-MoS_2 phase.

CN equals to 5.22 and the homopolar Mo–Mo bonds with a relatively broad BL distribution peaking at 2.9 Å with the partial CN reaching ≈2. These values are in excellent agreement with the fitted Mo K-edge experimental data suggesting that the MQ model well describes the local structure of the Mo atoms in a-MoS_2. In addition, a small quantity of homopolar S–S bonds was observed in the MQ model having a BL of 2.1 Å and a partial CN 0.11. The S–S BL agrees well with that of covalently bonded S atoms, which is calculated from the atomic radii of the S atoms; however, the presence of the homopolar S–S bonds to a lesser extent compared to the value obtained from XPS can be attributed to the difference between the as-deposited and MQ amorphous phases.[48] In addition, the total CN of S atoms is 2.71, which is ≈10% less than 3 in the crystalline phase, suggesting that a certain number of S atoms are two-fold coordinated. Note that the presence of such S atoms in the MQ phase suggests the existence of lone-pair electrons, which is a typical feature of amorphous chalcogenides.

To better understand the mechanism of the phase transition between a- and c-MoS_2, we performed subsequent "*in silico*" crystallization of the MQ-MoS_2 phase (details of this work will be published elsewhere). We found that the MQ-MoS_2 phase gradually transformed to the 1T′-MoS_2 phase rather than the 2H stable modification found experimentally (see Figure 6). This is understandable because the crystallization took place just below the melting point (to achieve crystallization on AIMD time scales). Indeed, electronically analogous $MoTe_2$ has a metastable high-temperature 1T′ phase. It is not unreasonable to assume that a similar phase can be formed for MoS_2 at elevated temperatures. The transition from the 1T′ to the 2H phase, taking place at a lower temperature, requires time scales inaccessible to AIMD.

https://doi.org/10.1021/acsanm.1c01504
ACS Appl. Nano Mater. 2021, 4, 8834–8844

The 1T′ phase is characterized (i) by the presence of a Mo−Mo BL of 2.9 Å, which is very similar to the Mo−Mo BLs in the amorphous phase; that is, the Mo−Mo bonds are preserved and (ii) the layers are buckled (*i.e.* not flat). The former may be the underlying reason why the 1T′ phase is initially formed from the amorphous phase. The buckling of the layers may be attributable to the positional and compositional disorder that still exists during the initial stages of crystallization into a 2D layered structure. We note here that a similar process, namely, the formation of the layered structure with the remaining local disorder, was also observed during the crystallization of a different 2D chalcogenide $Cr_2Ge_2Te_6$,[49,50] suggesting that this may be a typical feature of a 3D−2D crystallization process.

We would like to note that the layers in our crystallized MoS_2 model are less buckled than which would be expected for the 1T′ phase either due to the thermal effect (crystallization takes place at 1800 K) or because this is an intermediate phase between the 1T′ and 1T phases.[51] In this work, since the local arrangement is similar to the 1T′ phase, we use this term for the "in silico" crystallized MoS_2 phase.

Values obtained from the analysis of the MoS_2 models including the BL cutoffs used are summarized in Table 3.

Table 3. CNs and BLs of MQ Amorphous MoS_2 and Crystallized MoS_2 in 1T′ and 2H−MoS_2[a]

bonds	CN	BL/Å	cut off/Å
MQ-Mo−S	5.22	2.37	2.6
MQ-Mo−Mo	2	2.9	3
MQ-S−Mo	2.61	2.37	2.6
MQ-S−S	0.11	2.1	2.1
1T′-Mo−S1	3.1	2.37	2.45
1T′-Mo−S2	3.16	2.52	2.45−2.65
1T′-S1−Mo	1.55	2.37	2.45
1T′-S2−Mo	1.58	2.52	2.45−2.65
1T′-Mo−Mo	3.17	2.9	3.1
2H-Mo−S	6	2.37	2.6
2H-Mo−Mo	6	3.16	3.2
2H-S−Mo	3	2.37	2.4

[a]The 2H-MoS_2 phase, taken from a database, represents the final stable phase.

It is remarkable that a-MoS_2 crystallizes directly into a hexagonal layered structure with van der Waals gaps. This is in stark contrast to a different typical representative van der Waals crystal Sb_2Te_3, which initially crystallizes into a cubic phase with random distribution of vacancies, which subsequently form vacancy layers and van der Waals gaps.[52] We hypothesize that the observed direct transformation of a-MoS_2 into a layered structure could be the key point of the preferential crystal growth along the ⟨002⟩ axis even on nontemplating substrates. Therefore, we believe that crystallization of a thin film of a-MoS_2 is a promising approach to fabricate preferentially oriented thin films of c-MoS_2 in a large scale.

Experimentally, we could not observe the a-MoS_2 to 1T′ phase transformation; however, the crystallization process can be observed in $MoTe_2$,[24] where amorphous $MoTe_2$ first converts to the 1T′ phase and after long-term annealing above 600 °C gradually recrystallizes to 2H modification. Therefore, it can be assumed that the 1T′ phase appears to be an intermediate phase on the path between a-MoS_2 and 2H-MoS_2. This fact is also evident from the BL analyses shown in Figure 6A−I, which demonstrate that the broad distributions of the BLs in the MQ phase gradually narrow through the 1T′ to 2H phases. To prove this idea and at the same time to verify the quality of all MoS_2 models against the experimental data, we calculated Mo K-, S K-edge, and SL_3-edge XANES spectra for all three models using a FEFF code and compared them with experimentally recorded counterparts. Note that the valence band spectra (Figure 4F) clearly show that the crystallization process is accompanied by a strong influence on S 3p-Mo 4d hybridization, which justifies the possibility to examine SL_3-edge XANES spectra, which provide complementary information to the S K-edge data due to different selection rules. We would like to emphasize that, different from EXAFS, the XANES spectra provide three-dimensional structural information and therefore functions as an unmistakable fingerprint for each structure. Figure 7 shows (A, C, E) experimental and (B, D, F) calculated Mo K-edge, S K-edge, and SL_3-edge XANES spectra of amorphous and crystalline MoS_2. While the XANES spectra calculated for each of the 36 Mo atoms and 72 S atoms in the cluster of the MQ phase all differ, as to be expected for an amorphous material,[48] the corresponding average XANES spectra are in very good agreement with experimental curves considering both the positions and amplitudes of all features. Strikingly, an even more remarkable agreement in the XANES spectra can be observed between c-MoS_2 and the 2H-MoS_2 model, which are nearly identical. We thus conclude that the MQ and 2H-MoS_2 models properly represent the real a-MoS_2 and c-MoS_2 phases.

As mentioned before, the major change during crystallization can be monitored around the S atoms. In the case of the S K-edge, the so-called "white line" is more intense for the 2H phase, and at the same time, a new sharp peak appears directly above the white line in the 2H phase as a result of the coherent arrangement of atoms. One can notice that, compared to the 2H phase, the less pronounced peak right above the white line also exists in the 1T′ phase. However, the white-line intensity for the 1T′ phase is very similar to the MQ phase. It means that the two sets of the Mo−S bonds in the 1T′ phase significantly reduce the white-line intensity, which can help discriminate between the 1T′ and 2H phases using S K-edge XANES spectra. Similarly, using different selection rules for electronic transitions, the SL_3-edge XANES spectrum of the a-MoS_2 phase is characterized by a featureless prepeak and a smooth curve above the absorption edge. When the 2H phase is formed, characteristic peaks appear on both the pre-edge area and the rest of the XANES spectrum.

Last but not least, the corresponding XANES spectra for the 1T′ phase represent transient curves between the MQ and the 2H phases, which supports the idea that the 1T′ phase is an intermediate phase during the crystallization of a-MoS_2. We argue that this behavior may be general for all amorphous TMDCs.

Finally, we would like to point out that the experimental techniques used in this work examine the average structure of the studied area and they have some limitations. For example, using XRD, it is difficult to discern crystals with a size below 1−2 nm. Even molecular dynamics reveal a phase transformation within a periodically repeated cell and does not provide information on how crystals are oriented with respect to each other. To investigate crystallization of a-MoS_2 from the initial state, the use of transmission electron microscopy (TEM) is advantageous. We believe that it is worth discussing

https://doi.org/10.1021/acsanm.1c01504
ACS Appl. Nano Mater. 2021, 4, 8834−8844

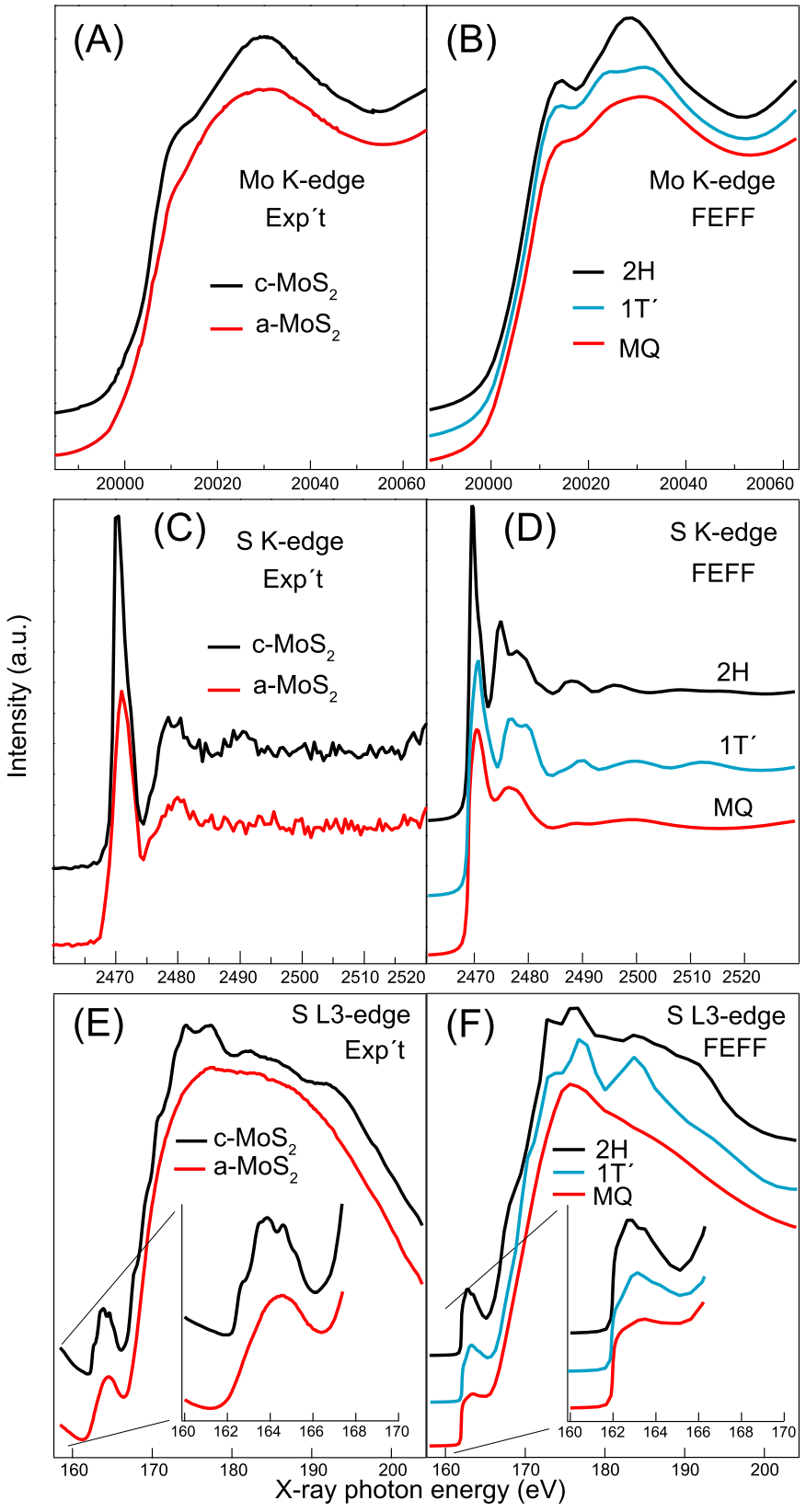

Figure 7. (Color online) (A,C,E) Experimental and (B,D,F) calculated Mo K-edge, S K-edge, and SL_3-edge XANES spectra of the amorphous and crystalline MoS_2 thin films.

our findings in connection with recently published results using this powerful technique. Detailed TEM probing of magnetron-sputtered a-MoS_2 on Si substrates preheated to 300 °C disclosed the presence of some MoS_2 crystals, which grew both parallel to the substrate (at the substrate/MoS_2 interface) up to 10 nm in thickness of MoS_2 and perpendicular to the substrate and deeper into the film.[53,54] Additional annealing of a-MoS_2 at 500 °C under vacuum generated crystals that randomly

https://doi.org/10.1021/acsanm.1c01504
ACS Appl. Nano Mater. 2021, 4, 8834−8844

oriented in the whole film, even at the interface.[53] The recent report on crystallization of amorphous MoS_2 studied by TEM shows that the perpendicular crystal growth of MoS_2 can be observed at 400 °C and the preferentially oriented crystals along the ⟨002⟩ crystallographic plane were exclusively formed above 780 °C.[55]

We believe that room temperature deposition has a strong impact on the amorphous character of the as-deposited a-MoS_2 films, and thus, the as-deposited a-MoS_2 described in the present work should be mainly free of these nanocrystals or their seeds. This opinion is corroborated by the SL_3-edge XANES spectra, which provide an unmistakable fingerprint for each structure. As discussed earlier, the SL_3-edge XANES spectrum of a-MoS_2 is very smooth, whereas characteristic peaks appear on the SL_3-edge XANES spectrum in the case of the 2H phase. These findings are in a perfect agreement with the TEM study of amorphous MoS_x and the 2H MoS_2 phase in combination with electron energy loss spectroscopy.[56] Second, in this work, we annealed the a-MoS_2 thin film at 800 °C, which should only lead to the formation of preferentially oriented crystals along the ⟨002⟩ crystallographic plane[55] rather than randomly oriented crystals or crystals perpendicularly grown on the substrate. In light of the obtained results, we believe that the fabrication of preferentially oriented c-MoS_2 thin films in 2H modification with a thickness of a few nanometers using the transformation of a thin a-MoS_2 layer is a promising approach providing a similar output as more complicated two-step preparation methods such as sulfidation of MoO_x.[57]

CONCLUSIONS

In conclusion, through a combination of experimental and theoretical studies, we presented a promising approach to fabricate crystalline MoS_2 *via* transformation of a thin amorphous layer of MoS_2 (which was singled out as the prototypical TMDC) examined in terms of long-range and short-range orders. We found that the structural analysis of both a-MoS_2 and c-MoS_2 *via* the XPS and XAS techniques is in excellent agreement with theoretical models. While the total CN for the Mo atoms is the same in both phases, ≈25% of the Mo atoms in a-MoS_2 forms homopolar Mo−Mo bonds, which can explain strong absorption of a-MoS_2 in the infrared spectral region. Next, we revealed the crystallization mechanism of a-MoS_2, where a-MoS_2 first converts to the 1T′ phase and, after long-term annealing, transforms to the stable 2H modification. We suppose that the observed transformation of three-dimensional a-MoS_2 into a layered structure is an intrinsic property of TMDCs and it could be the key point of preferential crystal growth along the ⟨002⟩ symmetry even on nontemplating substrates. The proposed approach demonstrates a simple and efficient way to fabricate thin 2D TMDCs for applications in nano- and optoelectronic devices.

AUTHOR INFORMATION

Corresponding Author

Milos Krbal − *Center of Materials and Nanotechnologies (CEMNAT), Faculty of Chemical Technology, University of Pardubice, 530 02 Pardubice, Czech Republic;* orcid.org/0000-0002-8317-924X; Phone: +420 466 037 404; Email: milos.krbal@upce.cz

Authors

Vit Prokop − *Center of Materials and Nanotechnologies (CEMNAT), Faculty of Chemical Technology, University of Pardubice, 530 02 Pardubice, Czech Republic*

Alexey A. Kononov − *Department of Physical Electronics, Herzen State Pedagogical University of Russia, St. Petersburg 191186, Russia*

Jhonatan Rodriguez Pereira − *Center of Materials and Nanotechnologies (CEMNAT), Faculty of Chemical Technology, University of Pardubice, 530 02 Pardubice, Czech Republic;* orcid.org/0000-0001-6501-9536

Jan Mistrik − *Center of Materials and Nanotechnologies (CEMNAT), Faculty of Chemical Technology, University of Pardubice, 530 02 Pardubice, Czech Republic; Institute of Applied Physics and Mathematics, Faculty of Chemical Technology, University of Pardubice, Pardubice 53210, Czech Republic*

Alexander V. Kolobov − *Department of Physical Electronics, Herzen State Pedagogical University of Russia, St. Petersburg 191186, Russia; Device Technology Research Institute, National Institute of Advanced Industrial Science and Technology, Tsukuba 305-8568 Ibaraki, Japan;* orcid.org/0000-0002-8125-1172

Paul J. Fons − *Device Technology Research Institute, National Institute of Advanced Industrial Science and Technology, Tsukuba 305-8568 Ibaraki, Japan; Faculty of Science and Technology, Department of Electronics and Electrical Engineering, Keio University, Yokohama, Kanagawa 223-8522, Japan*

Yuta Saito − *Device Technology Research Institute, National Institute of Advanced Industrial Science and Technology, Tsukuba 305-8568 Ibaraki, Japan;* orcid.org/0000-0002-9576-1560

Shogo Hatayama − *Department of Materials Science, Graduate School of Engineering, Tohoku University, Sendai 980-8579, Japan*

Yi Shuang − *Department of Materials Science, Graduate School of Engineering, Tohoku University, Sendai 980-8579, Japan*

Yuji Sutou − *Department of Materials Science, Graduate School of Engineering, Tohoku University, Sendai 980-8579, Japan;* orcid.org/0000-0002-3067-2727

Stepan A. Rozhkov − *Department of Physical Electronics, Herzen State Pedagogical University of Russia, St. Petersburg 191186, Russia*

Jens R. Stellhorn − *Department of Applied Chemistry, Graduate School of Advanced Science and Engineering, Higashi-Hiroshima, Hiroshima 739-8527, Japan*

Shinjiro Hayakawa − *Department of Applied Chemistry, Graduate School of Advanced Science and Engineering, Higashi-Hiroshima, Hiroshima 739-8527, Japan;* orcid.org/0000-0002-4187-6928

Igor Pis − *CNR-IOM, TASC Laboratory, 34149 Basovizza, Trieste, Italy;* orcid.org/0000-0002-5222-9291

Federica Bondino − *CNR-IOM, TASC Laboratory, 34149 Basovizza, Trieste, Italy;* orcid.org/0000-0001-6505-9319

Complete contact information is available at: https://pubs.acs.org/10.1021/acsanm.1c01504

Author Contributions

M.K., A.V.K., and P.F. conceived and designed the experiments. M.K. wrote the manuscript, measured XRD data,

https://doi.org/10.1021/acsanm.1c01504
ACS Appl. Nano Mater. 2021, 4, 8834−8844

analyzed EXAFS data, and calculated XANES spectra. V.P. was responsible for the sample deposition. J.M. probed optical properties. J.R.-P. carried out the XPS measurements. A.A.K., A.V.K., P.F., Yuta Saito, Shogo Hatayama, Yi Shuang, and Yuji Sutou measured Mo K-edge EXAFS data, J.R.S. and Shinjiro Hayakawa collected S K-edge XANES spectra, and I.P. and F.B. measured S $L_{2,3}$-edge XANES spectra. S.R. contributed to EXAFS data analyses. P.F. designed and performed AIMD simulations. A.V.K and P.F. helped with writing the manuscript. All authors discussed the results and commented on the manuscript.

Notes

The authors declare no competing financial interest.

■ ACKNOWLEDGMENTS

This work was supported by the Czech Science Foundation 19-17997S, LM2018103, the Russian Foundation for Basic Research [grant RFBR 19-07-00353 (study of the amorphous phase), and a joint RFBR-JSPS project supported by grants RFBR 20-52-50012 and JPJSBP120204815 (3D−2D crystallization)] and JSPS KAKENHI grant number 19H02619. XAS experiments were performed within 2019B1324 SPring8 and 20AG034 HiSOR proposals. I.P. and F.B. acknowledge funding from the EUROFEL project and Elettra Sincrotrone Trieste for providing access to synchrotron radiation facilities.

■ REFERENCES

(1) Wang, Q. H.; Kalantar-Zadeh, K.; Kis, A.; Coleman, J. N.; Strano, M. S. Electronics and optoelectronics of two-dimensional transition metal dichalcogenides. *Nat. Nanotechnol.* **2012**, *7*, 699−712.

(2) Kolobov, A. V.; Tominaga, J. *Two-dimensional Transition-Metal Dichalcogenides*; Springer Series in Materials Science; Springer International Publishing AG, 2016.

(3) Nam, H.; Oh, B.-R.; Chen, P.; Chen, M.; Wi, S.; Wan, W.; Kurabayashi, K.; Liang, X. Multiple MoS_2 transistors for sensing molecule interaction kinetics. *Sci. Rep.* **2015**, *5*, 10546.

(4) Buscema, M.; Island, J. O.; Groenendijk, D. J.; Blanter, S. I.; Steele, G. A.; van der Zant, H. S. J.; Castellanos-Gomez, A. Photocurrent generation with two-dimensional van der waals semiconductors. *Chem. Soc. Rev.* **2015**, *44*, 3691.

(5) Gourmelon, E.; Lignier, O.; Hadouda, H.; Couturier, G.; Bernède, J. C.; Tedd, J.; Pouzet, J.; Salardenne, J. MS_2 (M = W, Mo) photosensitive thin films for solar cells. *Sol. Energy Mater. Sol. Cells* **1997**, *46*, 115−121.

(6) Peng, W.-c.; Li, X.-y. Synthesis of MoS_2/g-C_3N_4 as a solar light-responsive photocatalyst for organic degradation. *Catal. Commun.* **2014**, *49*, 63−67.

(7) Mittal, H.; Khanuja, M. Optimization of $MoSe_2$ nanostructure by surface modification using conducting polymer for degradation of cationic and anionic dye: Photocatalysis mechanism, reaction kinetics and intermediate product study. *Dyes Pigm.* **2020**, *175*, 108109.

(8) Xie, J.; Zhang, H.; Li, S.; Wang, R.; Sun, X.; Zhou, M.; Zhou, J.; Lou, X. W. D.; Xie, Y. Defect-rich MoS_2 ultrathin nanosheets with additional active edge sites for enhanced electrocatalytic hydrogen evolution. *Adv. Mater.* **2013**, *25*, 5807−5813.

(9) Eftekhari, A. Molybdenum diselenide ($MoSe_2$) for energy storage, catalysis, and optoelectronics. *Appl. Mater. Today* **2017**, *8*, 1−17.

(10) Wang, T.; Chen, S.; Pang, H.; Xue, H.; Yu, Y. MoS_2-based nanocomposites for electrochemical energy storage. *Adv. Sci.* **2017**, *4*, 1600289.

(11) Tongay, S.; Zhou, J.; Ataca, C.; Lo, K.; Matthews, T. S.; Li, J.; Grossman, J. C.; Wu, J. Thermally driven crossover from indirect toward direct bandgap in 2D semiconductors: $MoSe_2$ versus MoS_2. *Nano Lett.* **2012**, *12*, 5576−5580.

(12) Nayak, A. P.; Yuan, Z.; Cao, B.; Liu, J.; Wu, J.; Moran, S. T.; Li, T.; Akinwande, D.; Jin, C.; Lin, J.-F. Pressure-modulated conductivity, carrier density, and mobility of multilayered tungsten disulfide. *ACS Nano* **2015**, *9*, 9117−9123.

(13) Duerloo, K.-A. N.; Li, Y.; Reed, E. J. Structural phase transitions in two-dimensional Mo- and W-dichalcogenide monolayers. *Nat. Commun.* **2014**, *5*, 4214.

(14) Kim, Y.; Bark, H.; Kang, B.; Lee, C. Wafer-scale substitutional doping of monolayer MoS_2 films for high-performance optoelectronic devices. *ACS Appl. Mater. Interfaces* **2019**, *11*, 12613−12621.

(15) Lei, Y.; Butler, D.; Lucking, M. C.; Zhang, F.; Xia, T.; Fujisawa, K.; Granzier-Nakajima, T.; Cruz-Silva, R.; Endo, M.; Terrones, H.; Terrones, M.; Ebrahimi, A. Single-atom doping of MoS_2 with manganese enables ultrasensitive detection of dopamine: Experimental and computational approach. *Sci. Adv.* **2020**, *6*, No. eabc4250.

(16) Novoselov, K. S.; Mishchenko, A.; Carvalho, A.; Castro Neto, A. H. 2D materials and van der waals heterostructures. *Science* **2016**, *353*, aac9439.

(17) Anto Jeffery, A.; Nethravathi, C.; Rajamathi, M. Two-dimensional nanosheets and layered hybrids of MoS_2 and WS_2 through exfoliation of ammoniated MS_2 (M = Mo,W). *J. Phys. Chem. C* **2014**, *118*, 1386−1396.

(18) Mattinen, M.; Hatanpää, T.; Sarnet, T.; Mizohata, K.; Meinander, K.; King, P. J.; Khriachtchev, L.; Räisänen, J.; Ritala, M.; Leskelä, M. Atomic layer deposition of crystalline MoS_2 thin films: New molybdenum precursor for low-temperature film growth. *Adv. Mater. Interfaces* **2017**, *4*, 1700123.

(19) Krbal, M.; Prikryl, J.; Zazpe, R.; Dvorak, F.; Bures, F.; Macak, J. M. 2D $MoSe_2$ structures prepared by atomic layer deposition. *Phys. Status Solidi RRL* **2018**, *12*, 1800023.

(20) Liu, K.-K.; Zhang, W.; Lee, Y.-H.; Lin, Y.-C.; Chang, M.-T.; Su, C.-Y.; Chang, C.-S.; Li, H.; Shi, Y.; Zhang, H.; Lai, C.-S.; Li, L.-J. Growth of large-area and highly crystalline MoS_2 thin layers on insulating substrates. *Nano Lett.* **2012**, *12*, 1538−1544.

(21) Hasani, A.; Van Le, Q.; Tekalgne, M.; Choi, M.-J.; Choi, S.; Lee, T. H.; Kim, H.; Ahn, S. H.; Jang, H. W.; Kim, S. Y. Fabrication of a WS_2/p-Si heterostructure photocathode using direct hybrid thermolysis. *ACS Appl. Mater. Interfaces* **2019**, *11*, 29910−29916.

(22) Tao, J.; Chai, J.; Lu, X.; Wong, L. M.; Wong, T. I.; Pan, J.; Xiong, Q.; Chi, D.; Wang, S. Growth of wafer-scale MoS_2 monolayer by magnetron sputtering. *Nanoscale* **2015**, *7*, 2497−2503.

(23) Pondick, J. V.; Woods, J. M.; Xing, J.; Zhou, Y.; Cha, J. J. Stepwise sulfurization from MoO_3 to MoS_2 via chemical vapor deposition. *ACS Appl. Nano Mater.* **2018**, *1*, 5655−5661.

(24) Huang, J.-H.; Hsu, H.-H.; Wang, D.; Lin, W.-T.; Cheng, C.-C.; Lee, Y.-J.; Hou, T.-H. Polymorphism control of layered $MoTe_2$ through two-dimensional solid-phase crystallization. *Sci. Rep.* **2019**, *9*, 8810.

(25) Simpson, R. E.; Krbal, M.; Fons, P.; Kolobov, A. V.; Tominaga, J.; Uruga, T.; Tanida, H. Toward the ultimate limit of phase change in $Ge_2Sb_2Te_5$. *Nano Lett.* **2010**, *10*, 414−419.

(26) Rodríguez-Carvajal, J. Recent advances in magnetic structure determination by neutron powder diffraction. *Phys. B* **1993**, *192*, 55−69.

(27) Ravel, B.; Newville, M. ATHENA, ARTEMIS, HEPHAESTUS: data analysis for X-ray absorption spectroscopy using IFEFFIT. *J. Synchrotron Radiat.* **2005**, *12*, 537−541.

(28) Kresse, G.; Hafner, J. Ab initiomolecular dynamics for liquid metals. *Phys. Rev. B: Condens. Matter Mater. Phys.* **1993**, *47*, 558.

(29) Perdew, J. P.; Burke, K.; Ernzerhof, M. Generalized Gradient Approximation Made Simple. *Phys. Rev. Lett.* **1996**, *77*, 3865−3868.

(30) Rehr, J. J.; Kas, J. J.; Vila, F. D.; Prange, M. P.; Jorissen, K. Parameter-free calculations of X-ray spectra with FEFF9. *Phys. Chem. Chem. Phys.* **2010**, *12*, 5503−5513.

(31) Whittingham, M. S.; Gamble, F. R., Jr. The lithium intercalates of the transition metal dichalcogenides. *Mater. Res. Bull.* **1975**, *10*, 363−371.

(32) Tonndorf, P.; Schmidt, R.; Schneider, R.; Kern, J.; Buscema, M.; Steele, G. A.; Castellanos-Gomez, A.; van der Zant, H. S. J.; de

https://doi.org/10.1021/acsanm.1c01504
ACS Appl. Nano Mater. 2021, 4, 8834−8844

Vasconcellos, S. M.; Bratschitsch, R. Single-photon emission from localized excitons in an atomically thin semiconductor. *Optica* **2015**, *2*, 347−352.
(33) Wu, F.; Qu, F.; MacDonald, A. H. Exciton band structure of monolayer MoS_2. *Phys. Rev. B: Condens. Matter Mater. Phys.* **2015**, *91*, 075310.
(34) Dory, J.-B.; Castro-Chavarria, C.; Verdy, A.; Jager, J.-B.; Bernard, M.; Sabbione, C.; Tessaire, M.; Fédéli, J.-M.; Coillet, A.; Cluzel, B.; Noé, P. Ge-Sb-S-Se-Te amorphous chalcogenide thin films towards on-chip nonlinear photonic devices. *Sci. Rep.* **2020**, *10*, 11894.
(35) Mott, N. F. *Electrons in Glass*. Nobel Lecture, 1977.
(36) Kastner, M.; Adler, D.; Fritzsche, H. Valence-alternation model for localized gap states in lone-pair semiconductors. *Phys. Rev. Lett.* **1976**, *37*, 1504.
(37) Pariari, D.; Varma, R. M.; Nair, M. N.; Zeller, P.; Amati, M.; Gregoratti, L.; Nanda, K. K.; Sarma, D. D. On the origin of metallicity and stability of the metastable phase in chemically exfoliated MoS_2. *Appl. Mater. Today* **2020**, *19*, 100544.
(38) Mondal, A.; Paul, A.; Srivastava, D. N.; Panda, A. B. Defect- and phase-induced acceleration of electrocatalytic hydrogen production by ultrathin and small MoS_2-decorated rGO sheets. *ACS Appl. Nano Mater.* **2018**, *1*, 4622−4632.
(39) Fleisch, T. H.; Mains, G. J. An XPS study of the UV reduction and photochromism of MoO_3 and WO_3. *J. Chem. Phys.* **1982**, *76*, 780.
(40) Gandubert, A. D.; Legens, C.; Guillaume, D.; Payen, E. X-ray photoelectron spectroscopy surface quantification of sulfided CoMoP catalysts. Relation between activity and promoted sites. Part II: Influence of the sulfidation temperature. *Surf. Interface Anal.* **2006**, *38*, 206−209.
(41) Scanlon, D. O.; Watson, G. W.; Payne, D. J.; Atkinson, G. R.; Egdell, R. G.; Law, D. S. L. Theoretical and experimental study of the electronic structures of MoO_3 and MoO_2. *J. Phys. Chem. C* **2010**, *114*, 4636−4645.
(42) Smart, R. S. C.; Skinner, W. M.; Gerson, A. R. XPS of sulphide mineral surfaces: metal-deficient, polysulphides, defects and elemental sulphur. *Surf. Interface Anal.* **1999**, *28*, 101−105.
(43) Chen, C. P.; Ong, B. L.; Ong, S. W.; Ong, W.; Tan, H. R.; Chai, J. W.; Zhang, Z.; Wang, S. J.; Pan, J. S.; Harrison, L. J.; Kang, H. C.; Tok, E. S. In-situ growth of HfO_2 on clean 2H-MoS_2 surface: Growth mode, interface reactions and energy band alignment. *Appl. Surf. Sci.* **2017**, *420*, 523−534.
(44) Pal, B.; Singh, A.; Sharada, G.; Mahale, P.; Kumar, A.; Thirupathaiah, S.; Sezen, H.; Amati, M.; Gregoratti, L.; Waghmare, U. V.; Sarma, D. D. Chemically exfoliated MoS_2 layers: Spectroscopic evidence for the semiconducting nature of the dominant trigonal metastable phase. *Phys. Rev. B* **2017**, *96*, 195426.
(45) Wu, L.; Longo, A.; Dzade, N. Y.; Sharma, A.; Hendrix, M. M. R. M.; Bol, A. A.; de Leeuw, N. H.; Hensen, E. J. M.; Hofmann, J. P. The origin of high activity of amorphous MoS_2 in the hydrogen evolution reaction. *ChemSusChem* **2019**, *12*, 4383−4389.
(46) Lassalle-Kaiser, B.; Merki, D.; Vrubel, H.; Gul, S.; Yachandra, V. K.; Hu, X.; Yano, J. Evidence from in Situ X-ray Absorption Spectroscopy for the Involvement of Terminal Disulfide in the Reduction of Protons by an Amorphous Molybdenum Sulfide Electrocatalyst. *J. Am. Chem. Soc.* **2015**, *137*, 314−321.
(47) Åsbrink, S.; Kihlborg, L.; Malinowski, M. High-pressure single-crystal X-ray diffraction studies of MoO_3. I. Lattice parameters up to 7.4 GPa. *J. Appl. Crystallogr.* **1988**, *21*, 960−962.
(48) Krbal, M.; Kolobov, A. V.; Fons, P.; Tominaga, J.; Elliott, S. R.; Hegedus, J.; Uruga, T. Intrinsic complexity of the melt-quenched amorphous $Ge_2Sb_2Te_5$ memory alloy. *Phys. Rev. B: Condens. Matter Mater. Phys.* **2011**, *83*, 054203.
(49) Hatayama, S.; Shuang, Y.; Fons, P.; Saito, Y.; Kolobov, A. V.; Kobayashi, K.; Shindo, S.; Ando, D.; Sutou, Y. Cr-triggered local structural change in $Cr_2Ge_2Te_6$ phase change material. *ACS Appl. Mater. Interfaces* **2019**, *11*, 43320−43329.
(50) Saito, Y.; Hatayama, S.; Shuang, Y.; Fons, P.; Kolobov, A. V.; Sutou, Y. Dimensional transformation of chemical bonding during crystallization in a layered chalcogenide material. *Sci. Rep.* **2021**, *11*, 4782.
(51) Friedman, A. L.; Hanbicki, A. T.; Perkins, F. K.; Jernigan, G. G.; Culbertson, J. C.; Campbell, P. M. Evidence for chemical vapor induced 2H to 1T phase transition in MoX_2 (X=Se, S) transition metal dichalcogenide films. *Sci. Rep.* **2017**, *7*, 3836.
(52) Chen, X.; Liu, X.; Cheng, Y.; Song, Z. The impact of vacancies on the stability of cubic phases in Sb-Te binary compounds. *NPG Asia Mater.* **2019**, *11*, 40.
(53) Moser, J.; Lévy, F. Growth mechanisms and near-interface structure in relation to orientation of MoS_2 sputtered thin films. *J. Mater. Res.* **1992**, *7*, 734−740.
(54) Ohashi, T.; Suda, K.; Ishihara, S.; Sawamoto, N.; Yamaguchi, S.; Matsuura, K.; Kakushima, K.; Sugii, N.; Nishiyama, A.; Kataoka, Y.; Natori, K.; Tsutsui, K.; Iwai, H.; Ogura, A.; Wakabayashi, H. Multi-layered MoS_2 film formed by high-temperature sputtering for enhancement-mode nMOSFETs. *Jpn. J. Appl. Phys.* **2015**, *54*, 04DN08.
(55) Fei, L.; Lei, S.; Zhang, W.-B.; Lu, W.; Lin, Z.; Lam, C. H.; Chai, Y.; Wang, Y. Direct TEM observations of growth mechanisms of two-dimensional MoS_2 flakes. *Nat. Commun.* **2016**, *7*, 12206.
(56) Lee, S. C.; Benck, J. D.; Tsai, C.; Park, J.; Koh, A. L.; Abild-Pedersen, F.; Jaramillo, T. F.; Sinclair, R. Chemical and Phase Evolution of Amorphous Molybdenum Sulfide Catalysts for Electrochemical Hydrogen Production. *ACS Nano* **2016**, *10*, 624−632.
(57) Hansen, L. P.; Johnson, E.; Brorson, M.; Helveg, S. Growth Mechanism for Single- and Multi-Layer MoS_2 Nanocrystals. *J. Phys. Chem. C* **2014**, *118*, 22768−22773.

https://doi.org/10.1021/acsanm.1c01504
ACS Appl. Nano Mater. 2021, 4, 8834−8844